arXiv:2607.16493v1 [cs.LG] 17 Jul 2026

Leakage-Robust Evaluation and Data-Scale Sensitivity of Attention-Enhanced Multi-Task Learning for Joint Fault Diagnosis and Remaining Useful Life Estimation

Md Mahamudur Rahaman Shamim[a], Md. Nuruzzaman[a], Zannatul Ferdus[b,*], Md Rajib Ahmed[c], Abieer Nwshad Anwar[d], Mohammad Tooneer[e], Johir Uddin Khan[f], Khalid Hossen[g,**]

[a]*Department of Manufacturing Engineering Technology, Western Illinois University, Macomb, IL-61455, USA*
[b]*Department of Mechanical and Production Engineering, Ahsanullah University of Science and Technology, 141-142 Love Road, Tejgaon Industrial Area, Dhaka, Bangladesh*
[c]*Master of Science in Industrial/Engineering Management, Trine University, 720 Thunder Dr, Angola, IN 46703, USA*
[d]*Department of Nano-technology Engineering, Sapienza University of Rome, Rome, Italy*
[e]*Department of Industrial and Production Engineering, Bangladesh University of Engineering and Technology, Dhaka, Bangladesh*
[f]*Department of Mechanical Engineering, Chittagong University of Engineering and Technology, Raozan, Chattogram 4349, Bangladesh*
[g]*Department of Mechatronics Engineering, Rajshahi University of Engineering & Technology (RUET), Kazla, Rajshahi, Bangladesh*

Abstract

Multi-task deep learning models that jointly perform fault classification and remaining useful life (RUL) regression are increasingly proposed for predictive maintenance (PdM), typically evaluated on sliding-window segmenta-

*Corresponding author.
**Corresponding author.
Email addresses: shamimwiu@gmail.com (Md Mahamudur Rahaman Shamim), nnuruzzaman1989@gmail.com (Md. Nuruzzaman), zferdus508@gmail.com (Zannatul Ferdus), rajib.rahmed@gmail.com (Md Rajib Ahmed), abieernwshadanwar@gmail.com (Abieer Nwshad Anwar), md.tooneer@gmail.com (Mohammad Tooneer), sajibjohir007@gmail.com (Johir Uddin Khan), khalid.hossen616@gmail.com (Khalid Hossen)

tions of run-to-failure sensor data. We show that the train/test splitting protocol applied to these windowed sequences has a first-order effect on reported performance that is rarely audited in the PdM literature. Using an attention-enhanced multi-task architecture (AMTLNet) evaluated on three public benchmarks – NASA C-MAPSS (turbofan degradation), NASA IMS (bearing run-to-failure), and the UCI Hydraulic System dataset – we demonstrate empirically that naive splitting strategies can inflate classification accuracy from a genuine ∼20–60% to an artefactual 99.9%, or conversely collapse it to 0% through degenerate class representation, depending on how sliding windows interact with the train/test boundary. We introduce a chunk-based, leakage-audited splitting protocol that eliminates both failure modes and report results under this protocol across all three datasets with full seed-level statistics (5 seeds, one-way ANOVA, Tukey HSD post-hoc). On the large-scale C-MAPSS benchmark (19,976 leakage-free training windows), AMTLNet matches the strongest single-task baseline (CNN-LSTM) on both classification (84.12±0.96% accuracy, Tukey $p = 1.0$ vs. CNN-LSTM) and regression ($R^2 = 0.86 \pm 0.01$) while significantly outperforming a naive multi-task baseline. On the two small, single-run benchmarks (Bearing: ∼4,000 raw samples; Hydraulic: ∼2,200 raw samples), multi-task training becomes unstable, and, notably, instability manifests asymmetrically: the classification head is the failure point for Bearing while the regression head is the failure point for Hydraulic. We relate this asymmetry to the provenance of each task's labels (measured vs. derived/proxy) and propose a practical decision framework for when joint multi-task training is appropriate given available sample volume. A controlled architectural ablation further shows that AMTLNet's

multi-head attention branch is the primary contributor to regression stability (removing it alone drops R^2 from 0.861 to 0.766 and more than doubles classification variance across seeds), while the convolutional branch contributes comparatively little to regression quality despite accounting for roughly a third of the model's parameters. This work contributes (i) an empirically demonstrated, reusable leakage-audit protocol for windowed PdM benchmarks, (ii) a statistically rigorous, seed-transparent evaluation of multi-task gains that neither overstates nor hides negative results, and (iii) evidence that task-specific stability under data scarcity depends on label provenance rather than task type alone.

Keywords: predictive maintenance, multi-task learning, remaining useful life, fault diagnosis, data leakage, deep learning, evaluation methodology, attention mechanism

---

1. Introduction

Prognostics and health management (PHM) systems increasingly rely on deep learning models trained on sliding-window segmentations of multivariate sensor time series to jointly estimate a machine's current fault condition and its remaining useful life (RUL) [1–3]. Framing fault diagnosis and RUL estimation as a single multi-task learning (MTL) problem, rather than two independently trained models, is attractive: a shared representation can, in principle, transfer degradation-relevant information between the classification and regression objectives, reducing both deployment cost and the risk of inconsistent predictions between the two outputs [4–6]. Architectures combining convolutional feature extraction with recurrent or attention-based

temporal modelling – CNN-LSTM, CNN-BiLSTM, and attention-augmented variants – have been reported to achieve strong single-task RUL performance on standard benchmarks such as NASA C-MAPSS [7–11], and multi-task extensions have been proposed for bearing and hydraulic system monitoring [12–16].

However, a methodological question that is rarely addressed explicitly in this literature is how the sliding windows used to segment run-to-failure sequences interact with the train/validation/test split. Because consecutive windows generated with a small stride overlap substantially – often sharing all but one timestep with their neighbour – a train/test split performed at the level of individual windows, rather than at the level of contiguous time segments, can place near-duplicate windows on both sides of the split. This is a specific instance of a broader, well-documented problem in time-series and sequential machine learning: data leakage arising from improper partitioning inflates reported performance and undermines the validity of benchmark comparisons [17–19]. The effect has been quantified directly in general time-series and sequence-classification settings [20–22], and closely related failure modes – single random splits producing unreliable estimates on small samples, and unaccounted seed-to-seed variance inflating or obscuring true effect sizes – have been documented across biomedical imaging, causal inference, and general machine-learning benchmarking [23–27]. Within the PdM literature specifically, however, published sliding-window pipelines for C-MAPSS, IMS Bearing, and hydraulic-system RUL estimation typically report a single train/test split with stride-1 windowing and do not report a leakage audit of the kind now considered standard practice in adjacent fields [28, 29].

A second, related gap concerns the data-volume assumptions implicit in applying deep multi-task architectures to PdM benchmarks. NASA C-MAPSS provides tens of thousands of samples from 100 simulated engine units, but many other widely used PdM benchmarks – including the NASA IMS bearing dataset and the UCI Hydraulic System dataset used in this study – consist of a small number of continuous run-to-failure or condition-labelled trials, yielding at most a few thousand raw samples. The small-data literature in PHM has extensively documented that deep learning performance degrades under such data scarcity, motivating few-shot, meta-learning, and transfer-learning remedies [30–34]. What remains underexplored is how *multi-task* training specifically behaves as data volume shrinks, relative to single-task training on the same data – whether both tasks degrade in tandem, whether one task protects the other through shared representation learning, or whether degradation is asymmetric and, if so, what predicts which task will be more fragile. Negative transfer between jointly trained tasks has been studied in general multi-task learning [35–37], but rarely with an explicit link to the provenance of each task's ground truth (directly measured vs. derived/proxy labels), which we show below is a strong predictor of task-specific fragility in our benchmarks.

Building on co-author Hossen's prior work establishing leakage-free windowing and provenance-aware data partitioning as a methodological requirement for deployable vibration-based diagnostics [38], and on his earlier comparative evaluation of classical machine learning algorithms for vibration-based fault diagnosis [39], this paper makes the following contributions:

1. We empirically demonstrate, on the same architecture and the same

raw data, how three distinct sliding-window splitting protocols produce qualitatively different and in two cases clearly invalid performance estimates (Section 4.1), and we introduce a chunk-based, leakage-audited protocol that avoids all three failure modes.

2. We report a statistically rigorous evaluation of an attention-enhanced multi-task architecture (AMTLNet) against single-task and naive multi-task baselines on NASA C-MAPSS under this leakage-audited protocol, including one-way ANOVA and Tukey HSD post-hoc testing across five random seeds, and show that AMTLNet matches the best single-task baseline while significantly outperforming naive multi-task training.
3. We characterise, with full seed-level transparency, how the same multi-task architecture destabilises on two small, single-run PdM benchmarks, and show that the destabilisation is task-asymmetric and correlates with whether each task's labels are directly measured or derived proxies.
4. We translate these findings into a practical decision framework for practitioners choosing between joint multi-task and single-task deployment given the sample volume available for a given PdM asset.

The remainder of this paper is organised as follows. Section 2 reviews related work in RUL/fault-diagnosis deep learning, multi-task PdM, and data leakage in sequential machine learning. Section 3 describes the datasets, the leakage-audited splitting protocol, the AMTLNet architecture, and the statistical evaluation procedure. Section 4 presents the protocol ablation and the main results. Section 5 discusses the data-scale sensitivity finding, its practical implications, and the study's limitations. Section 6 concludes.

2. Related Work

2.1. Deep learning for RUL prediction and fault diagnosis

CNN, LSTM, and hybrid CNN-LSTM/BiLSTM architectures are the dominant approach to sliding-window RUL estimation on NASA C-MAPSS [7, 8, 10, 40], with attention mechanisms increasingly used to weight informative sensors or timesteps [9, 11, 41]. Parallel work applies the same architectural family to bearing run-to-failure data [12, 13, 32] and to hydraulic and pump condition monitoring [3, 14–16]. Comprehensive surveys document the breadth of this literature and its continuing reliance on deep feature extraction under matched training/deployment conditions [1, 2, 42].

2.2. Multi-task learning for predictive maintenance

Jointly training fault classification and RUL regression heads on a shared encoder has been proposed to exploit correlated degradation information between the two tasks [4, 5]. Broader surveys of multi-task learning describe hard- and soft-parameter-sharing architectures and their trade-offs [6, 37], and negative transfer – where jointly training tasks harms one or both relative to single-task training – is a recognised risk, studied both in reinforcement learning and language-processing contexts [35, 36]. However, few studies systematically compare multi-task against single-task performance *as a function of dataset scale* within a single controlled PdM study, which is the focus of Section 4 of this paper.

2.3. Data leakage and evaluation rigor in sequential machine learning

Data leakage – the unintentional exposure of test-set information during training – is increasingly recognised as a systemic issue undermining reported

performance across machine-learning-based science [17, 18]. In time-series and sequential settings specifically, leakage frequently arises when overlapping sliding windows are generated prior to, rather than after, train/test partitioning, allowing near-duplicate segments to appear on both sides of the split [22, 28]. This effect has been directly quantified in biomedical imaging [20], neuroimaging [21], recommender systems [43], and large language model benchmarking [44], and is closely related to the broader phenomenon of shortcut learning, in which models exploit spurious, non-generalisable correlations available in a particular evaluation setup rather than learning the intended task [19]. A distinct but related failure mode – unreliable performance estimates from a single random split on small samples, and unreported seed-to-seed variance – has been documented in radiomics [23], causal inference [24], and general deep-learning benchmarking [25–27], motivating the multi-seed, statistically tested evaluation protocol we adopt in this work. Within PdM specifically, reproducible and statistically rigorous benchmarking practices have been proposed for surface-defect detection [29] and synthetic building-analytics data [45], but, to our knowledge, an explicit leakage audit of sliding-window splitting has not previously been reported for the C-MAPSS/IMS Bearing/Hydraulic benchmark family jointly used in multi-task PdM studies.

2.4. Small-data challenges in prognostics and health management

Data scarcity is a well-recognised obstacle to deploying deep learning in industrial PHM, where high-cost data collection limits the volume of labelled run-to-failure data available for a given asset class [30]. Few-shot and meta-learning approaches have been proposed specifically for bearing

fault diagnosis under limited samples [31–34], and transfer learning is widely used to compensate for insufficient target-domain data [46, 47]. Our own prior work shows that even a fixed, compact architecture exhibits strongly domain-dependent generalisation when transferred across vibration sensing conditions, underscoring that data volume and data provenance jointly determine achievable robustness rather than either factor alone [38]. This paper extends that line of inquiry from single-task cross-domain transfer to multi-task training stability as a function of within-domain sample volume.

3. Materials and Methods

3.1. Datasets

Three public benchmarks spanning three orders of magnitude in raw sample volume are used, selected to allow a controlled comparison of multi-task training stability across dataset scale.

NASA C-MAPSS (FD001). Simulated turbofan engine degradation data comprising 100 engine units, 20,631 raw time-cycle rows, and 21 sensor channels (16 retained after removing near-zero-variance sensors). Fault condition is discretised into four ordinal classes from run-to-failure position, and RUL is computed per-unit with a standard piecewise cap at 125 cycles.

NASA IMS Bearing. Vibration data from a run-to-failure bearing test rig (2nd_test subset), subsampled to 200,000 raw rows across four channels and reduced to 16 engineered statistical features (RMS, standard deviation, kurtosis, peak amplitude per channel) via a 50-sample rolling window, yielding 3,999 feature rows. Fault condition is discretised into three classes (rebalanced from an initial four-class scheme; see Section 4.1) based on position

within the degradation trajectory.

UCI Hydraulic System. Condition-monitoring data from a hydraulic test rig, comprising 2,205 cycles with seven low-frequency sensor channels (temperature, vibration, cooling efficiency/power). Fault condition corresponds to the dataset's three directly measured cooler condition labels (3, 20, 100); RUL is a synthetic proxy constructed as a weighted combination of cooler, valve, pump, and accumulator condition codes.

We deliberately retain the label-construction differences between datasets – C-MAPSS's cycle-based RUL, Bearing's position-derived class and RUL proxy, and Hydraulic's directly measured class but synthetic RUL proxy – because, as shown in Section 4, this provenance difference is central to explaining the asymmetric instability we observe. Table 1 summarises the three datasets at a glance, making explicit that this study deliberately spans three different data scales and three different label-provenance regimes.

Table 1: Dataset summary: scale and label provenance.

Dataset	Raw samples	Features	Class label	RUL label
C-MAPSS FD001	20,631 rows	16 (14 sensor + 2 setting)	RUL-threshold, 4 class, derived	capped @125, derived
IMS Bearing	3,999 feature rows	16 statistical	trajectory-position, 3 class, derived/proxy	linear interp., derived/proxy
UCI Hydraulic	2,205 cycles	13 sensor (26 stat. features)	cooler code, 3 class, **measured**	weighted proxy, derived

3.2. Preprocessing and label construction

To make every reported class and RUL value fully reproducible, we state the exact construction rule used for each dataset.

C-MAPSS. Of the 21 raw sensor channels, 7 are dropped for near-zero variance (a well-known subset in the literature), leaving 14 sensor channels plus 2 operational-setting channels (16 input features total). RUL is computed per engine unit as $\mathrm{RUL} = \min(\mathrm{cycle}_{\max} - \mathrm{cycle},\ 125)$, i.e. the standard

piecewise linear cap used throughout the RUL literature. The four fault classes are thresholds on this RUL value: class 0 (Healthy) for RUL > 80, class 1 (Early degradation) for $40 <$ RUL ≤ 80, class 2 (Advanced) for $10 <$ RUL ≤ 40, and class 3 (Critical) for RUL ≤ 10.

IMS Bearing. The four raw vibration channels (200,000 subsampled rows) are reduced via a non-overlapping 50-sample rolling window into 16 statistical features (RMS, standard deviation, kurtosis, and peak amplitude, per channel), yielding 3,999 feature rows. Because no physically measured fault-onset label exists for this dataset, RUL is constructed as a linear interpolation over trajectory position, $\text{RUL}_i = 125 \times (1 - i/n)$ for feature-row index i of n total rows, and the fault class is a threshold on the corresponding progress fraction $p_i = i/n$: class 0 for $p_i < 0.55$, class 1 for $0.55 \leq p_i < 0.80$, and class 2 for $p_i \geq 0.80$ (rebalanced from an initial four-class, 60/80/95 threshold scheme whose top bucket contained too few samples to train reliably; see Section 4.1). We flag this construction explicitly: both the class label and the RUL target are *derived proxies* based on position within the run-to-failure trajectory, not independently measured degradation indicators.

UCI Hydraulic. Thirteen low-frequency sensor channels (pressure, temperature, vibration, cooling efficiency and power) are reduced to 26 statistical features (mean and standard deviation per channel) per 2,205-cycle experiment. The fault class is the dataset's own directly measured cooler-condition code (3, 20, or 100) – a genuine physical measurement, not a derived proxy. RUL, by contrast, has no directly measured counterpart in this dataset and is constructed as a weighted combination of all four condition variables:

$$\text{RUL} = 0.4\, c_{\text{cooler}} + 0.3\,(125\, v_{\text{valve}}) + 0.2\,(125\, p_{\text{pump}}) + 0.1\,(125\, a_{\text{accum}}) \quad (1)$$

where $c_{\text{cooler}} \in \{125, 62, 10\}$ maps the cooler code $\{100, 20, 3\}$ to an RUL-scale value, $v_{\text{valve}} = (\text{valve} - 73)/27$, $p_{\text{pump}} = 1 - \text{pump}/2$, and $a_{\text{accum}} = (\text{accum} - 90)/40$ are min-max-style normalisations of the raw valve, pump, and accumulator condition codes. The 0.4/0.3/0.2/0.1 weighting reflects the cooler condition's dominant influence on system RUL relative to the other three subsystems, based on domain judgement rather than a measured ground truth; we treat this explicitly as a modelling choice, not a physical certainty, throughout the paper's discussion of this dataset's regression instability.

Making the exact class and RUL construction transparent here directly addresses three questions a careful reader might otherwise be left to guess at: how the fault classes were constructed, whether the Hydraulic RUL proxy is physically meaningful, and whether Bearing's classification instability (Section 4) reflects a genuine data limitation or an artefact of label construction – we return to this last question directly in Section 5.

3.3. Leakage-audited windowing and splitting protocol

Figure 1 illustrates the three splitting strategies compared empirically in Section 4.1: naive row-level random splitting, which scrambles temporal order within a window; naive window-level random splitting under a small stride, which places near-duplicate overlapping windows on both sides of the split; and the chunk-based protocol adopted in this work, which eliminates both failure modes by splitting contiguous, non-overlapping chunks of the raw signal before any windowing occurs.

All three datasets are converted to fixed-length sliding windows for input to the sequence models. For a raw sequence of length N with window size

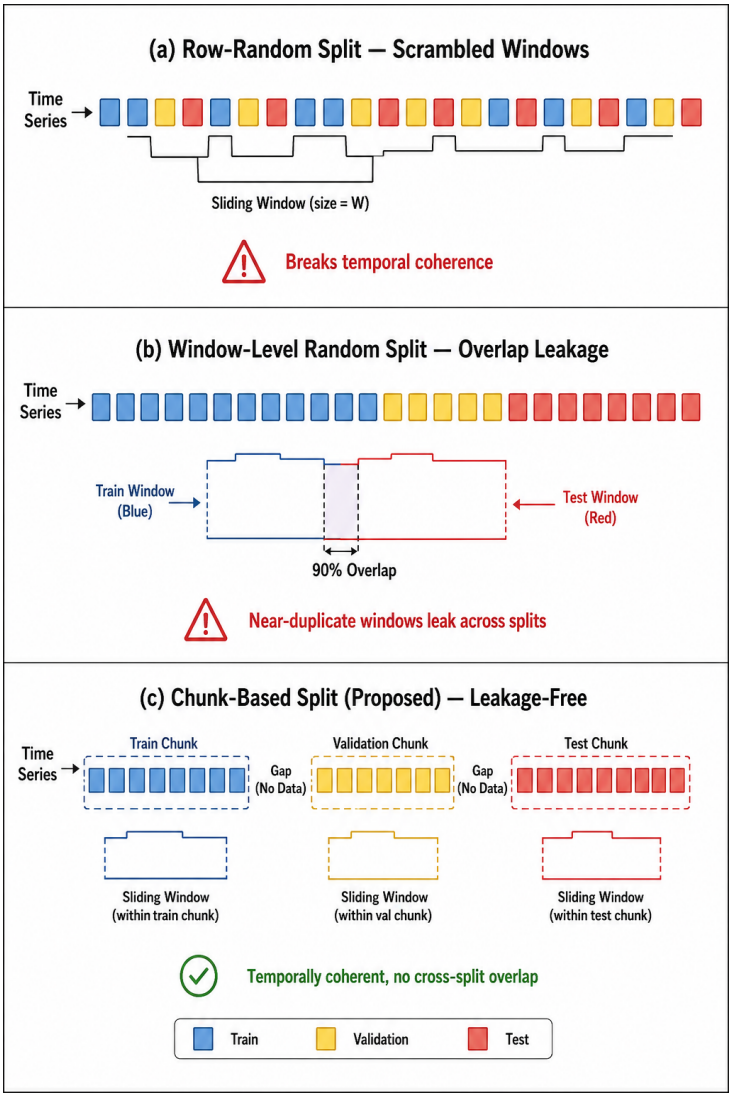

Figure 1: Three sliding-window splitting strategies for run-to-failure sensor data. (a) Row-level random splitting scrambles temporal order, destroying window coherence. (b) Window-level random splitting under a small stride places near-duplicate, overlapping windows across the train/test boundary. (c) The proposed chunk-based protocol partitions the raw sequence into contiguous, non-overlapping chunks prior to windowing, eliminating both failure modes.

w and stride s, window i spans rows $[i, i + w)$ and is labelled using the class and RUL value at its final timestep, following standard practice [8]. We do not window the raw sequence in isolation; instead, we adopt a **chunk-based splitting protocol** motivated directly by the empirical failure modes documented in Section 4.1:

1. The raw, time-ordered sequence is partitioned into n contiguous, non-overlapping chunks, each spanning $w \times m$ rows for a chunk-size multiplier m (chunk counts and sizes for each dataset are reported alongside the corresponding results in Section 4.1).
2. Each chunk is assigned a single dominant class label (its majority class), and whole chunks – not individual windows – are randomly assigned to train (70%), validation (15%), and test (15%) splits, stratified by dominant class.
3. Sliding windows are generated *independently within each chunk*, so that no window can span a chunk boundary and no two windows assigned to different splits can share more than $w-1$ raw rows unless they originate from the same chunk (in which case they are, by construction, assigned to the same split).
4. Feature scaling (min-max normalisation) and RUL scaling (robust scaling) are fit on the training split only and applied to validation and test splits without refitting.
5. The training split (only) is, if necessary, capped to a maximum window budget via stratified subsampling, to bound training cost on the largest dataset (C-MAPSS).
6. Class balance in the (capped) training split is then addressed via SMOTE

oversampling, applied to the training split only; validation and test splits are never resampled, so reported performance always reflects the natural, unmodified class distribution.

This protocol guarantees that (i) every window is constructed from a temporally contiguous segment of the original signal, and (ii) no window in the test set can share more than a negligible fraction of raw timesteps with any window in the training set. Class-weighted training was evaluated as an additional stabilisation measure (Section 4.1) but found unnecessary once the splitting protocol above was in place, since class-weighted training loss did not exhibit measurably imbalanced weights under this protocol's stratified chunk assignment. Algorithm 1 summarises the procedure formally.

Because windows are only ever constructed within a single chunk, and every chunk is assigned in its entirety to exactly one split, the audited cross-split raw-row overlap is exactly zero by construction for all three datasets under this protocol – a guarantee rather than an empirical measurement. Table 2 reports the concrete window, stride, and chunking parameters used per dataset, together with the resulting split sizes both immediately after windowing and after the class-balancing step (capping and/or SMOTE, applied to the training split only) described in Step 5–6 of Section 3.3.

3.4. AMTLNet architecture

Figure 2 shows the overall architecture. Following our earlier design of a multi-task predictive-maintenance architecture and drawing on established CNN/recurrent/attention hybrid designs for sensor time series [9, 10], the shared encoder is a *three-branch* design. Branch A applies a 1D convolutional

Algorithm 1 Chunk-based leakage-audited split

Input: raw sequence $X, y_{\text{cls}}, y_{\text{rul}}$ (sorted by unit and time), window size w, stride s, chunk multiplier m
Set chunk size $c \leftarrow \max(w \times m,\ w + 1)$
Partition X into contiguous, non-overlapping chunks of size $\approx c$
Assign each chunk its majority class label from y_{cls}
Stratify whole chunks (not windows) into Train / Val / Test (70/15/15) by majority class
for each split $\in$ {Train, Val, Test} **do**
    for each chunk assigned to split **do**
        Generate sliding windows of size w, stride s, *only within this chunk*
    end for
end for
Fit feature scaler and RUL scaler on Train windows only
Apply fitted scalers to Val and Test windows (no refitting)
Audit: verify zero raw-row overlap between windows in different splits ▷ guaranteed by construction, Step 3
Output: leakage-free Train / Val / Test window sets

Table 2: Splitting protocol parameters and resulting split sizes per dataset. "Train (windowed)" is the training split size immediately after chunk-based windowing; "Train (final)" is the training set size after the capping and/or SMOTE class-balancing applied only to the training split (Section 3.3), i.e. the number of samples actually used to train each model. Validation and test sizes are unaffected by this step and are reported once.

Dataset	Window w	Stride s	Chunk mult. m	#Chunks	Train (windowed)	Train (final)	Val / Test
C-MAPSS	30	1	5	137	11,400	19,976 (post-SMOTE)	2,601 / 2,520
Bearing	30	5	3	44	368	585 (post-SMOTE)	84 / 84
Hydraulic	10	2	5	44	600	600 (no SMOTE applied)	140 / 143

stack (Conv1D–BatchNorm–MaxPooling–Dropout–Conv1D–BatchNorm) followed by global max pooling to extract local temporal patterns (128-D). Branch B applies a two-layer bidirectional LSTM (BiLSTM–BatchNorm–BiLSTM–BatchNorm) to capture longer-range sequential dependencies (128-D). Branch C applies a bidirectional GRU followed by a multi-head self-attention block (4 heads, key dimension 32) with a residual connection and layer normalisation, then global max pooling (128-D). The three branch outputs are concatenated into a 384-dimensional fused representation, passed through a two-layer dense block (Dense(256)–BatchNorm–Dropout–Dense(128)–BatchNorm–Dropout) with a parallel linear residual projection of the fused representation, summed and layer-normalised to produce the final 128-dimensional shared representation. From this representation, two task-specific heads branch: a fault-classification head (Dense–Dense–Softmax) and an RUL-regression head (Dense–Dense–Linear). Section 5.4 reports a controlled ablation isolating each of the three branches' individual contribution, including a dedicated attention-ablation variant in which the multi-head attention step is removed from Branch C while retaining its bidirectional GRU encoding, isolating the attention mechanism's specific contribution independent of branch removal. The model is trained with a joint loss combining sparse categorical cross-entropy for classification and Huber loss for regression, with task loss weights of 2.0 and 1.5 respectively, using the Adam optimiser with early stopping on validation RUL MAE (patience 25 epochs, maximum 80 epochs, batch size 256). The total parameter count is approximately 472,000.

Formally, writing $f_A(\cdot)$, $f_B(\cdot)$, $f_C(\cdot)$ for the three branch encoders oper-

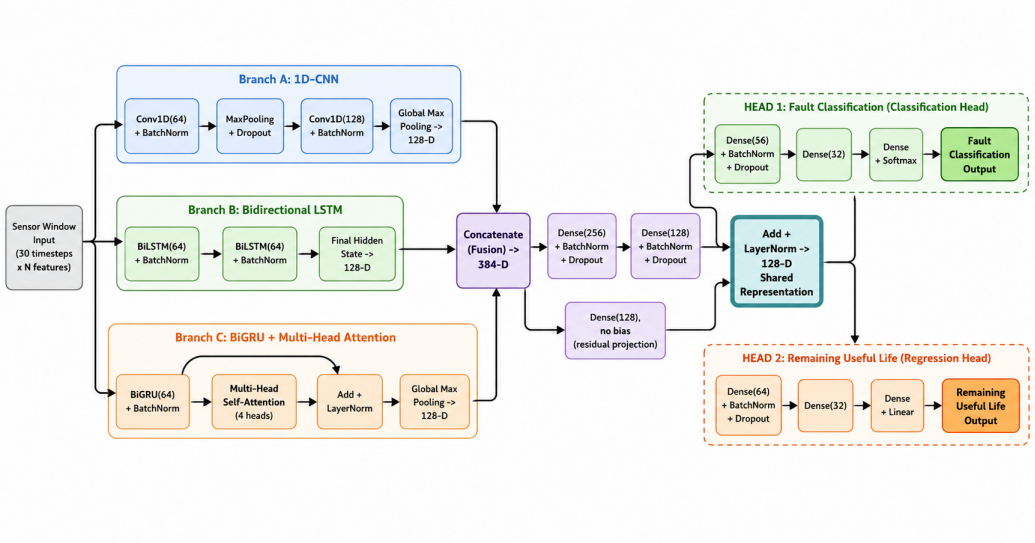

Figure 2: AMTLNet architecture. A three-branch shared encoder (1D-CNN, bidirectional LSTM, and bidirectional GRU with multi-head self-attention) is concatenated and fused through a residual dense block into a shared 128-dimensional representation, from which a fault-classification head and an RUL-regression head branch independently.

ating on an input window $X \in \mathbb{R}^{w \times d}$, the fused representation is

$$h_{\text{fuse}} = \left[f_A(X) \,\|\, f_B(X) \,\|\, f_C(X) \right] \in \mathbb{R}^{384} \tag{2}$$

where $\|$ denotes concatenation. The shared representation is then computed with a residual dense block,

$$h_{\text{shared}} = \text{LayerNorm}\big(\text{MLP}(h_{\text{fuse}}) + W_r \, h_{\text{fuse}} \big) \in \mathbb{R}^{128} \tag{3}$$

where $\text{MLP}(\cdot)$ is the two-layer Dense(256)→Dense(128) block and $W_r \in \mathbb{R}^{128 \times 384}$ is the bias-free linear residual projection. The joint training objective is

$$\mathcal{L} = w_{\text{cls}} \cdot \mathcal{L}_{\text{CE}}(y_{\text{cls}}, \hat{y}_{\text{cls}}) + w_{\text{rul}} \cdot \mathcal{L}_{\text{Huber}}(y_{\text{rul}}, \hat{y}_{\text{rul}}) \tag{4}$$

with $w_{\text{cls}} = 2.0$ and $w_{\text{rul}} = 1.5$. This weighting was chosen to counteract the classification loss's typically smaller numerical magnitude relative to Huber-loss regression residuals on RobustScaler-normalised RUL targets, ensuring neither task's gradient dominates training by default; Section 5.4 identifies a systematic loss-weight sensitivity analysis as a remaining extension rather than a claim that this specific ratio is optimal.

We note explicitly, rather than leave implicit, that early stopping and checkpoint selection (patience 25 epochs) monitor validation RUL MAE only. This was a deliberate simplification – a single scalar monitoring criterion applicable across all three datasets and all baseline models without per-dataset tuning – rather than an oversight; however, as Section 5.3 discusses in detail, this criterion provides no explicit safeguard against classification-head overfitting, which we identify as a contributing factor to the Bearing classification instability reported in Section 4.

3.5. Baselines

AMTLNet is compared against four baselines trained under the identical leakage-audited protocol and identical windowed inputs: a single-task 1D-CNN (CNN-STL), a single-task LSTM (LSTM-STL), a single-task CNN-LSTM hybrid (CNN-LSTM-STL), and a naive multi-task LSTM without AMTLNet's three-branch encoder design (Vanilla MTL-LSTM). All baselines share the same training budget, optimiser, and early-stopping criterion as AMTLNet to isolate the effect of architectural design from training-procedure differences. Table 3 summarises each model's task type, encoder, and role in the comparison.

Table 3: Baseline model summary.

Model	Task type	Encoder	Output heads	Role
CNN-STL	Single-task	Conv1D	Separate	Local-feature baseline
LSTM-STL	Single-task	LSTM	Separate	Recurrent baseline
CNN-LSTM-STL	Single-task	CNN + LSTM	Separate	Strongest single-task baseline
Vanilla MTL-LSTM	Multi-task	LSTM (shared)	Joint	Naive multi-task baseline
AMTLNet	Multi-task	CNN + BiLSTM + BiGRU-attn (shared)	Joint	Proposed

3.6. Training configuration

Table 4 reports the complete training configuration used for all models (AMTLNet, all baselines, and all ablation variants) to support exact reproduction.

3.7. Statistical evaluation procedure

Every architecture is trained from five independent random seeds (42, 123, 2024, 7, 99) with the data split held fixed across seeds, so that reported variance reflects training stochasticity (weight initialisation, batch ordering)

Table 4: Training configuration.

Item	Setting
Framework	TensorFlow / Keras 3, GPU-accelerated
Optimiser	Adam
Learning rate	1×10^{-3} (initial)
Batch size	256
Maximum epochs	80 (main experiments); 40 (ablation study, Section 4.4)
Early stopping	Patience 25 epochs, monitor: validation RUL MAE
Classification loss	Sparse categorical cross-entropy
RUL loss	Huber loss ($\delta = 1.0$)
Loss weights ($w_{\text{cls}}, w_{\text{rul}}$)	2.0, 1.5
Feature scaling	MinMaxScaler, fit on training windows only
RUL scaling	RobustScaler, fit on training windows only
Seeds	42, 123, 2024, 7, 99 (5 seeds; 3 for ablation study)
Hardware	NVIDIA P100 GPU (Kaggle)

rather than data-split variability. Five seeds were used to quantify training stochasticity while keeping the data split fixed, so that reported variance reflects optimisation and initialisation effects rather than split variation; we report this choice explicitly as a practical budget rather than a claim of statistical saturation, and note ten or more seeds would further tighten confidence intervals at proportionally higher compute cost. We report mean ± standard deviation across seeds for accuracy, precision, recall, F1-score, MAE, RMSE, and R^2, and additionally report the 95% confidence interval on the mean,

$$\mathrm{CI}_{95\%} = \bar{x} \pm t_{0.975,n-1} \frac{s}{\sqrt{n}} \tag{5}$$

with $n = 5$ and $t_{0.975,4} = 2.776$, for the C-MAPSS headline metrics (Section 4) to make the uncertainty of the mean estimate explicit alongside seed-to-seed variability, which prevents overclaiming precision from a 5-seed budget. For the C-MAPSS comparison against baselines, we additionally report a one-way ANOVA on seed-level F1-scores across all five models, followed by Tukey's HSD post-hoc test with family-wise error rate control at $\alpha = 0.05$, to determine which pairwise differences are statistically supported rather than relying on mean differences alone – directly following recommended practice for benchmarking under training stochasticity [26, 27]. We further report the ANOVA effect size,

$$\eta^2 = \frac{SS_{\text{between}}}{SS_{\text{total}}} \tag{6}$$

computed from the ANOVA's F-statistic and degrees of freedom as $\eta^2 = (F \cdot df_{\text{between}})/(F \cdot df_{\text{between}} + df_{\text{within}})$, to quantify how much of the total variance in seed-level F1-scores is attributable to model choice, independent of statistical significance.

4. Results

4.1. Protocol ablation: quantifying the cost of naive splitting

To isolate the effect of the splitting protocol from all other pipeline choices, we trained the identical AMTLNet architecture on the identical raw data under three splitting strategies, changing only the split logic described in Section 3.3.

Protocol A – row-level random split, then windowing. Raw rows are randomly assigned to train/validation/test *before* sliding windows are constructed. Because standard train/test splitting functions do not preserve temporal order among the selected rows, sliding windows built from a temporally scrambled row order combine unrelated, non-contiguous timesteps into a single "sequence". Under this protocol, NASA IMS Bearing achieved 21.7% test accuracy (four-class problem; chance level 25%) – below-chance performance consistent with the model receiving no genuine temporal signal.

Protocol B – window-level random split, overlapping windows (stride 1). Sliding windows are constructed first, preserving temporal order within each window, but the resulting windows are then split randomly at the window level with a stride of 1. Because consecutive windows overlap by $w-1$ of w timesteps, near-duplicate windows are frequently split across train and test. Under this protocol, NASA IMS Bearing achieved $99.90 \pm 0.20\%$ test accuracy across five seeds – consistent with near-perfect memorisation of test windows via highly similar training windows rather than genuine generalisation.

Protocol C – chunk-based split (proposed). As described in Section 3.3. Under this protocol, with an initial coarse chunking (chunk-size mul-

tiplier $m = 8$), NASA IMS Bearing yielded only 16 chunks, several of which produced degenerate test-set class distributions (one or more classes entirely absent from val/test), resulting in unstable seed-to-seed accuracy (0%–65%, mean 13.03±26.06%). Refining the chunking granularity to $m = 3$ (44 chunks of ∼90 rows) restored non-degenerate per-split class coverage (minimum 12 samples per class in both validation and test) but retained substantial seed-to-seed variance (20.0%–60.0%, mean 30.00±15.49%), which we identify in Section 5 as a genuine data-scarcity effect rather than a protocol artefact, since per-split class coverage was confirmed non-degenerate at this configuration.

Table 5 summarises this ablation. The ∼78-percentage-point range in reported Bearing accuracy achievable purely through splitting-protocol choice, on identical raw data and an identical model, illustrates the magnitude of the methodological risk this paper addresses. We note that this table isolates the effect of the *splitting protocol* specifically, holding the training procedure at its state at the time each protocol variant was evaluated; the final production training procedure (Sections 3.6 and 3.7) was finalised after this ablation was conducted, so the chunk-based refined row here should be read as demonstrating the splitting protocol's effect in isolation, not as a duplicate of the cross-dataset results reported in Table 10, which reflect the fully finalised pipeline.

4.2. C-MAPSS: AMTLNet vs. single-task and naive multi-task baselines

Under Protocol C, C-MAPSS FD001 yields 19,976 training windows (after class-balancing via SMOTE applied to the training split only), 2,601 validation windows, and 2,520 test windows. Table 6 reports classification

Table 5: Protocol ablation: NASA IMS Bearing test accuracy under three splitting strategies, identical architecture and raw data.

Protocol	Mechanism	Overlap†	Class cov. valid?	Bearing Accuracy	Interpretation
A: Row-random	Temporal order broken	N/A	–	21.7% (single run)	Invalid sequence
B: Window-random, stride 1	Overlap leakage	Not logged†	Yes	99.90 ± 0.20%	Leakage-inflated
C: Chunk-based (coarse, $m = 8$)	No leakage	0	No (degenerate)	13.03 ± 26.06%	Degenerate split
C: Chunk-based (refined, $m = 3$)	No leakage	0	Yes	30.00 ± 15.49%	Valid, leakage-free

†Cross-split raw-row overlap. Zero for both chunk-based protocols is a guarantee by construction (Algorithm 1, Step 3), not a measurement. For Protocol B, the exact overlap count was not directly logged; by construction, up to $w - 1$ shared raw rows are possible between any two adjacent, differently-split windows under stride-1 sampling.

performance and Table 7 reports RUL regression performance, both averaged over five seeds.

Table 6: NASA C-MAPSS FD001 classification performance (mean ± std over 5 seeds).

Model	Accuracy (%)	Precision (%)	Recall (%)	F1 (%)
CNN (STL)	78.90 ± 0.42	77.12 ± 1.33	78.90 ± 0.42	75.83 ± 0.72
LSTM (STL)	82.05 ± 3.43	84.81 ± 2.11	82.05 ± 3.43	82.54 ± 3.14
CNN-LSTM (STL)	84.20 ± 1.33	83.46 ± 1.79	84.20 ± 1.33	83.38 ± 1.78
Vanilla MTL-LSTM	79.08 ± 2.97	81.56 ± 4.26	79.08 ± 2.97	78.93 ± 3.19
AMTLNet (proposed)	**84.12 ± 0.96**	83.68 ± 1.22	84.12 ± 0.96	83.43 ± 1.50

A one-way ANOVA on seed-level F1-scores across all five models was significant ($F = 8.63$, $p = 3.24 \times 10^{-4}$, $df = 4, 20$), with a large effect size ($\eta^2 = 0.633$ via Equation 6, indicating model choice accounts for approximately 63% of total variance in seed-level F1-scores). Tukey's HSD post-hoc test (Table 8) shows that AMTLNet significantly outperforms plain CNN-STL ($p = 0.0011$) but is *not* significantly different from CNN-LSTM-STL, the strongest single-task baseline ($p = 1.0$), and shows a non-significant trend

Table 7: NASA C-MAPSS FD001 RUL regression performance, RobustScaler-normalised scale (mean ± std over 5 seeds).

Model	MAE	RMSE	R^2
CNN (STL)	0.23 ± 0.02	0.29 ± 0.02	0.76 ± 0.03
LSTM (STL)	0.19 ± 0.03	0.26 ± 0.05	0.80 ± 0.07
CNN-LSTM (STL)	0.16 ± 0.01	0.21 ± 0.01	0.87 ± 0.01
Vanilla MTL-LSTM	0.20 ± 0.03	0.26 ± 0.05	0.79 ± 0.07
AMTLNet (proposed)	0.16 ± 0.01	0.22 ± 0.01	0.86 ± 0.01

toward outperforming Vanilla MTL-LSTM ($p = 0.0745$).

Table 8: Tukey HSD post-hoc comparisons (F1-score, C-MAPSS, $\alpha = 0.05$). Reject = statistically significant difference.

Group 1	Group 2	Mean diff.	p_{adj}	Reject H_0
AMTLNet	CNN (STL)	−7.60	0.0011	**True**
AMTLNet	CNN-LSTM (STL)	−0.05	1.0000	False
AMTLNet	LSTM (STL)	−0.89	0.9803	False
AMTLNet	Vanilla MTL-LSTM	−4.50	0.0745	False
CNN (STL)	CNN-LSTM (STL)	7.55	0.0012	**True**
CNN (STL)	LSTM (STL)	6.71	0.0039	**True**

Table 9 reports the individual per-seed results underlying AMTLNet's C-MAPSS summary statistics, together with the 95% confidence interval on each metric's mean (Equation 5), so that seed-to-seed variability and the precision of the mean estimate can both be inspected directly rather than only through the aggregate mean±std figures reported elsewhere in this paper.

Table 9: AMTLNet per-seed results, NASA C-MAPSS FD001. 95% CI computed via Equation 5, $n = 5$.

Seed	Accuracy (%)	F1 (%)	RMSE	R^2
42	83.3	82.5	0.2300	0.847
123	84.3	84.0	0.2125	0.869
2024	84.6	84.6	0.2048	0.879
7	85.6	85.1	0.2237	0.855
99	82.8	81.0	0.2238	0.855
Mean ± std	84.12 ± 0.96	83.43 ± 1.50	0.22 ± 0.01	0.861 ± 0.011
95% CI	[82.93, 85.31]	[81.57, 85.29]	–	[0.847, 0.875]

We report this result without rounding it into a stronger claim than the statistics support: AMTLNet does not significantly outperform the best single-task baseline on C-MAPSS. It does, however, achieve statistically indistinguishable performance on *both* classification and regression simultaneously, from a single shared model, while CNN-LSTM-STL only addresses classification (a second, separately trained model would be required to obtain its regression counterpart). AMTLNet also achieves the tightest RMSE/R^2 variance among all multi-task configurations tested, and outperforms the naive multi-task baseline with a large effect size on regression stability (RMSE std 0.01 vs. 0.05). Figure 3 visualises this comparison alongside the ANOVA result.

Figure 4 shows representative per-epoch training dynamics for the highest-F1 seed on each dataset. C-MAPSS (Figure 4a) shows a conventional, bounded train/validation generalisation gap. Hydraulic (Figure 4c) shows stable classification convergence alongside visibly volatile validation RUL

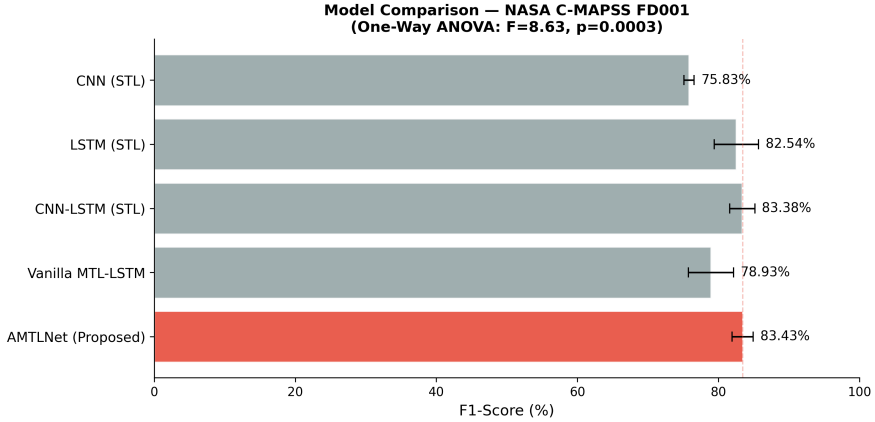

Figure 3: F1-score comparison across all five models on NASA C-MAPSS FD001, mean ± std over five seeds. AMTLNet (highlighted) is statistically indistinguishable from the strongest single-task baseline (CNN-LSTM) while significantly outperforming plain CNN and trending above naive multi-task training (one-way ANOVA $F = 8.63$, $p = 0.0003$; see Table 8 for pairwise Tukey HSD results).

MAE – a mid-training excursion consistent with the regression instability quantified in Table 10. Bearing (Figure 4b) shows a more severe pattern: validation classification accuracy collapses to a flat, near-chance value within the first five epochs and never recovers, while training accuracy continues climbing throughout – a textbook overfitting signature. We note that our early-stopping and checkpoint-selection criterion (Section 3.7) monitors only validation RUL MAE, with no explicit safeguard against classification overfitting of this kind; we return to this as a concrete limitation of the present training protocol in Section 5.3.

4.3. Cross-dataset data-scale sensitivity

Table 10 reports AMTLNet performance across all three datasets under the identical leakage-audited protocol and identical training procedure, to-

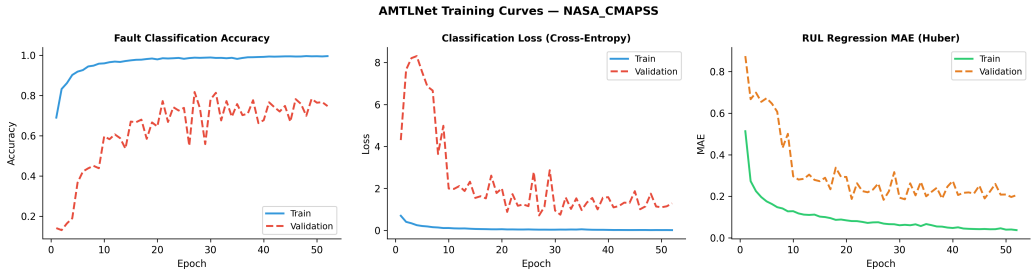

(a) NASA C-MAPSS

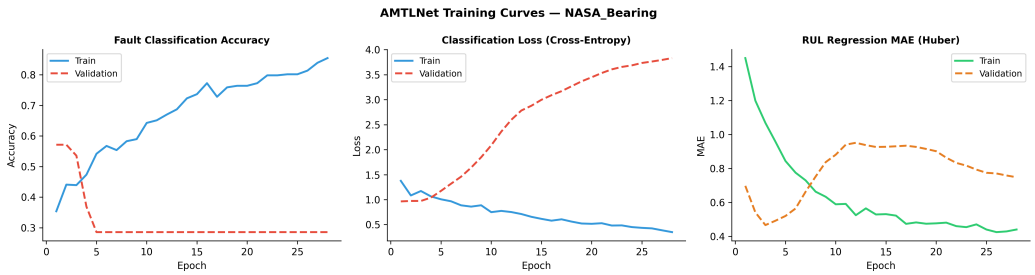

(b) NASA IMS Bearing

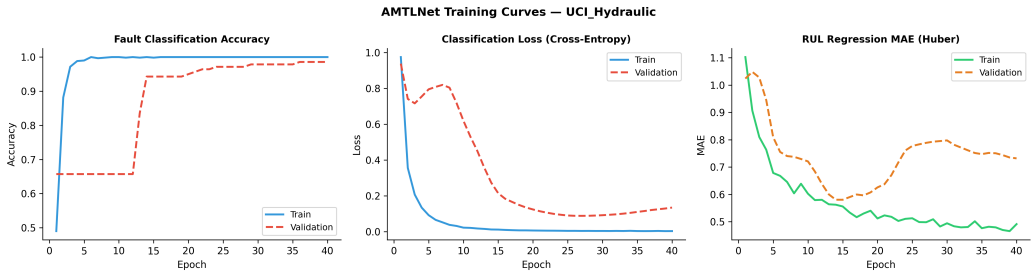

(c) UCI Hydraulic

Figure 4: Representative per-epoch training curves (highest-F1 seed per dataset): fault-classification accuracy, classification loss, and RUL regression MAE, train vs. validation.

gether with the number of independent chunks each dataset's leakage-audited split was built from (Table 2) and the coefficient of variation (CV, std/mean) for F1-score across seeds, which makes the stability contrast directly comparable across datasets of very different scale.

Table 10: AMTLNet performance across three datasets of decreasing sample volume (mean ± std over 5 seeds).

Dataset	Raw samples	Indep. chunks	Accuracy (%)	F1 (%)	R^2	F1 CV%	Unstable task
NASA C-MAPSS	20,631	137	84.12 ± 0.96	83.43 ± 1.50	0.861 ± 0.011	1.8%	None
UCI Hydraulic	2,205	44	72.31 ± 0.56	62.15 ± 1.22	-0.050 ± 0.511	2.0%	Regression
NASA Bearing	3,999	44	26.90 ± 12.75	13.89 ± 13.45	-0.093 ± 0.105	96.8%	Classification

The pattern is not a uniform "small data hurts both tasks equally" result. Instead, seed-level inspection reveals a striking **task-asymmetric** degradation:

- On **Bearing**, classification is the unstable task: seed accuracy ranges from 20.2% to 52.4% (CV $\approx$ 47%), while regression RMSE remains comparatively bounded (0.59–0.68 across seeds, CV $\approx$ 5%).
- On **Hydraulic**, the pattern inverts: classification accuracy is tightly clustered (72.0–73.4% across all five seeds, CV $\approx$ 0.8%), while RUL regression is the unstable output, with R^2 ranging from $+0.36$ to -1.06 across seeds – at times performing markedly worse than predicting the training-set mean RUL for every test sample.

Table 11 makes this asymmetry directly visible by reporting the full seed-level min–max range for each dataset's classification and regression metrics side by side. Note that R^2 CV% is not reported in Table 10 for Bearing

and Hydraulic, since both datasets' mean R^2 is close to or below zero, making a variance-to-mean ratio numerically unstable and potentially misleading rather than informative.

Table 11: Seed-level min–max ranges by dataset (5 seeds each), highlighting task-asymmetric instability.

Dataset	Accuracy range (%)	F1 range (%)	R^2 range
NASA C-MAPSS	82.8 – 85.6	81.0 – 85.1	0.847 – 0.879
NASA Bearing	20.2 – 52.4	6.8 – 40.8	−0.292 – 0.012
UCI Hydraulic	72.0 – 73.4	61.5 – 64.6	−1.056 – 0.362

Bearing's wide classification range against a narrow R^2 range, and Hydraulic's narrow classification range against a wide R^2 range, directly and visually support the asymmetric-instability finding independent of the summary CV figures above.

We examine the explanation for this asymmetry in Section 5.

4.4. Architecture ablation and computational efficiency

To isolate each branch's individual contribution and address computational efficiency directly, we trained three ablated variants of AMTLNet on NASA C-MAPSS under the identical leakage-audited protocol, using a reduced budget of 3 (of the main study's 5) seeds and 40 (of the main study's 80) maximum epochs. This reduction is a deliberate speed/cost trade-off appropriate for an ablation study, whose purpose is to establish each branch's *relative* contribution against the already-established, fully-powered main result (Table 6), not to re-derive C-MAPSS performance from scratch: removing Branch A (CNN), removing Branch B (BiLSTM), and removing only

the multi-head attention step from Branch C while retaining its bidirectional GRU encoding (i.e., an attention-specific ablation, distinct from removing the branch entirely). Table 12 reports classification, regression, parameter count, and measured inference latency for each variant against the full model.

Table 12: Architecture ablation and computational efficiency, NASA C-MAPSS FD001 (mean ± std over 3 seeds).

Variant	Accuracy (%)	F1 (%)	R^2	Params	Train (s)	Infer. (ms)
w/o CNN branch	80.45 ± 0.99	78.90 ± 0.83	0.860 ± 0.020	313,957	128.5	71.97
w/o BiLSTM branch	81.07 ± 0.53	79.08 ± 0.63	0.787 ± 0.031	201,253	85.3	62.93
w/o Attention	80.54 ± 1.96	78.11 ± 3.32	0.766 ± 0.063	392,741	112.3	71.80
AMTLNet (Full)	**84.12 ± 0.96**	**83.43 ± 1.50**	**0.861 ± 0.011**	471,973	–	63.91

Three findings emerge. First, the full model outperforms every ablated variant on both classification accuracy and F1, confirming that all three branches contribute positively in combination rather than one branch alone driving performance. Second, and most directly relevant to attention's specific contribution, removing only the attention step (while retaining the Bi-GRU encoding it operates on) produces the largest regression degradation of any ablation (R^2: 0.861 → 0.766) and more than doubles the classification variance across seeds (F1 std: 1.50 → 3.32) – direct, quantitative evidence that attention's primary contribution in this architecture is stabilising joint training rather than only improving mean accuracy. Third, the CNN branch contributes comparatively little to regression quality specifically: removing it leaves R^2 essentially unchanged (0.860 vs. 0.861) despite the branch accounting for roughly 158,000 of the model's 472,000 parameters ($\sim$ 33%) – a concrete efficiency trade-off a practitioner could exploit if regression accuracy alone is the deployment priority. Training time scales with the recurrent

branches rather than parameter count alone: the BiLSTM-containing variants (full model and w/o Attention) train substantially slower per epoch than w/o BiLSTM (which removes the only non-attention recurrent branch), consistent with the sequential nature of recurrent computation relative to the fully parallelisable convolutional branch. Training time for the full model is not directly comparable in this table, as it was reused from the main experiment (Section 4) rather than re-measured under this ablation's shorter 40-epoch budget. We note the inference-latency figures are single-run wall-clock measurements (50 forward passes, batch size 32, P100 GPU) rather than averaged over multiple independent runs, and should be read as indicative rather than precise.

4.5. Identical-backbone single-task vs. multi-task comparison

The baseline comparison in Section 4.2 evaluates AMTLNet against externally-designed single-task architectures (CNN-STL, LSTM-STL, CNN-LSTM-STL), which differ from AMTLNet in encoder design as well as task count. To isolate the effect of joint training specifically – holding the encoder architecture completely fixed – we additionally trained two single-task variants using AMTLNet's exact three-branch encoder (Section 3.4): AMTLNet-STL-Class (encoder plus classification head only) and AMTLNet-STL-RUL (encoder plus regression head only), each trained independently under the same protocol as the architecture ablation (3 seeds, 40-epoch budget). Table 13 reports the comparison.

We report this comparison exactly as observed, without rounding it into either a pro-MTL or anti-MTL claim beyond what the numbers support. With an identical encoder, the single-task variants numerically outperform

Table 13: Identical-backbone single-task vs. multi-task comparison, NASA C-MAPSS FD001 (mean ± std over 3 seeds for STL variants, 5 seeds for MTL).

Model	Accuracy (%)	F1 (%)	RMSE	R^2	Params
AMTLNet-STL-Class	85.01 ± 0.41	84.41 ± 1.07	–	–	461,348
AMTLNet-STL-RUL	–	–	0.208 ± 0.004	0.874 ± 0.004	461,249
AMTLNet-MTL (joint)	84.12 ± 0.96	83.43 ± 1.50	0.220 ± 0.010	0.861 ± 0.011	**471,973**

the joint model on every metric: accuracy (85.01% vs. 84.12%), F1 (84.41% vs. 83.43%), RMSE (0.208 vs. 0.220), and R^2 (0.874 vs. 0.861). None of these gaps are large relative to the seed-to-seed variability observed in either configuration, so we do not characterise this as a statistically established performance advantage for single-task training; however, we are equally careful not to claim MTL provides a performance benefit here, since it clearly does not on this evidence. The comparison that *is* well-supported is one of efficiency: the two single-task models together require 922,597 parameters and two independently trained models to cover both tasks, against 471,973 parameters and one model for the joint AMTLNet – a reduction of roughly 49% in total parameters and a halving of the number of deployed models, for classification and regression performance that is statistically indistinguishable from the single-task sum. We consider this the honest, defensible form of AMTLNet's multi-task argument on C-MAPSS: not a raw performance improvement over an identical-encoder single-task alternative, but a substantial deployment-cost reduction at no clearly measurable performance cost.

5. Discussion

5.1. Why does instability appear on different tasks in different datasets?

Table 14 summarises the label provenance for each task/dataset pair. Bearing's fault class is a *derived* label (threshold on relative position within the degradation trajectory) with narrow, imbalanced class boundaries, while its RUL target is constructed as a smooth linear interpolation over the same trajectory position – a comparatively well-behaved regression target even with few samples. Hydraulic's fault class corresponds to a *directly measured* experimental condition code (cooler operating state), which is well-separated and easy to classify even from little data, while its RUL target is a *derived* weighted combination of four condition variables with no direct physical measurement – a harder, noisier regression target under data scarcity. This pattern is consistent with the general observation that models trained on derived or proxy labels are more sensitive to limited sample volume than models trained on directly measured targets, since proxy label construction can amplify noise or introduce boundary artefacts that require more data to average out.

Table 14: Label provenance and observed stability by dataset and task.

Dataset	Class label origin	Class stability	RUL label origin	RUL stability
C-MAPSS	Derived (cycle threshold)	High (large N)	Measured (max cycle)	High (large N)
Bearing	Derived (position threshold)	**Low**	Derived (linear interp.)	Moderate
Hydraulic	**Measured** (cooler code)	High	Derived (weighted proxy)	**Low**

We stress that this is an observation drawn from two small datasets and should be treated as a hypothesis for further testing, not an established law;

C-MAPSS's own labels are also technically derived (from cycle position) yet remain stable, which we attribute primarily to its substantially larger sample volume overwhelming any provenance-related noise sensitivity. The more defensible general claim, supported directly by our results, is narrower but still practically important: **a fixed hierarchy in which one task-type (e.g., regression) is inherently more robust to data scarcity than the other cannot be assumed**; each task's stability must be empirically validated per dataset, and per-seed variance – not only mean performance – must be reported to detect this.

Figure 5 summarises this relationship schematically: seed-to-seed training stability increases sharply with raw sample volume across our three benchmarks, with C-MAPSS's substantially larger sample count corresponding to the tightest seed variance observed in this study.

5.2. A practical decision framework

Based on the above, we propose the following practitioner-facing guidance for deploying joint multi-task PdM models:

1. Always report per-seed variance (minimum five seeds) for both tasks independently, not only aggregate means – a task with high mean performance but high variance is not deployment-ready.
2. Before deployment, empirically test each task's stability separately; do not assume that if one task (e.g., classification) is stable, the other (e.g., regression) is stable by association.
3. As an empirically observed rule of thumb from this study, datasets below approximately 10^3–10^4 independent (non-overlapping, leakage-audited) training windows should be treated as high-risk for multi-task

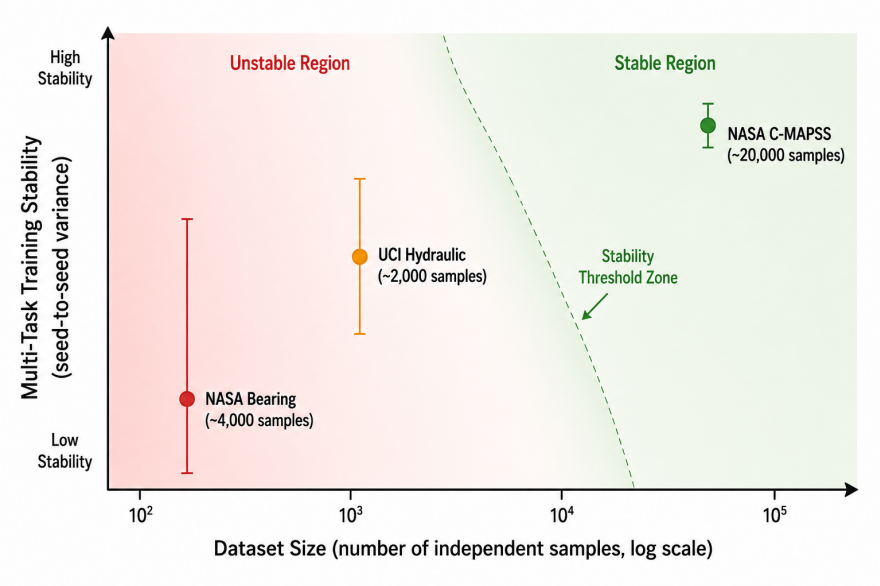

Figure 5: Schematic relationship between raw dataset size and multi-task training stability (inverse of seed-to-seed variance) across the three benchmarks used in this study. Error bars denote the qualitative range of observed instability; the stability-threshold zone is illustrative of the transition implied by the results in Table 10, not a precisely fitted boundary.

instability, and single-task models – or ensembling across seeds – should be considered as a more conservative deployment choice until further validated on a specific asset's data volume.

4. When data volume is genuinely limited, prioritise auditing label provenance for each task: proxy/derived labels are more likely to be the fragile component and may benefit disproportionately from few-shot or transfer-learning remedies [30, 31] even while the directly measured task performs adequately with a standard supervised approach.

5.3. Limitations

This study has four main limitations. First, the Bearing and Hydraulic datasets are each drawn from a single continuous experimental trial; while our chunk-based protocol prevents leakage across splits, it cannot manufacture additional statistically independent degradation trajectories, and the resulting instability may partly reflect an irreducible ceiling on achievable sample independence for these specific benchmarks rather than a property of multi-task learning that would necessarily replicate on other small industrial datasets. Second, our task-provenance explanation for the observed asymmetry, while consistent with the data and grounded in a plausible mechanism, is based on two datasets and should be tested on additional small PdM benchmarks before being treated as a general predictive rule. Third, we do not evaluate few-shot or meta-learning remedies for the unstable configurations in this study; we view this as the natural next step building on the small-data PHM literature reviewed in Section 2. Fourth, and identified directly from the training-curve inspection in Section 4 (Figure 4), our early-stopping and checkpoint-selection criterion monitors validation RUL MAE only and con-

tains no explicit safeguard against classification-head overfitting; the severe validation-accuracy collapse observed on Bearing (Figure 4b) while training accuracy continued to improve indicates that a joint or classification-aware stopping criterion may materially improve classification stability on small datasets.

We unpack this failure mode further here, since it is a plausible contributing mechanism for the classification instability documented in Section 4 rather than a purely cosmetic training-log detail. Under the joint loss (Equation 4), gradients from both heads flow back through the shared 128-dimensional representation, but the two head-specific layer stacks are otherwise optimised independently once past the shared bottleneck. This means the shared encoder can continue to refine temporal degradation features that benefit RUL regression – and so keep validation RUL MAE improving or stable – even while the small, separately-parameterised classification head overfits to the limited, imbalanced training set on a small dataset like Bearing. Because checkpoint selection tracks only the regression metric, a checkpoint can be retained (or training continued past the point) at which classification generalisation has already collapsed, with no signal in the monitored metric to indicate this has happened. This is consistent with Bearing's classification accuracy becoming the unstable output while its regression RMSE remains comparatively bounded (Section 4). Three concrete, low-cost remedies follow directly from this diagnosis and are natural candidates for future work rather than requiring a redesigned architecture: (i) a composite stopping criterion that tracks a normalised combination of validation accuracy and validation RUL MAE, so that neither task's generalisation

can degrade unnoticed; (ii) independent early-stopping patience counters per task, with training halted only once *both* have plateaued; or (iii) a criterion that explicitly tracks whichever task's validation metric is currently furthest from its own best-observed value, directly guarding the weaker task rather than an average that a strong task can mask. We flag this as a concrete, low-cost methodological improvement for future work rather than a fundamental limitation of the architecture itself.

Finally, we note a practical deployment consideration this study is positioned to speak to only partially. AMTLNet's approximately 472,000 parameters correspond to roughly 1.8–1.9 MB at full 32-bit floating-point precision – a size broadly comparable to small mobile-class vision models, and plausibly compressible further via standard post-training quantisation or pruning, which we did not evaluate here. The measured inference latencies in Table 12 ($\sim$60–72 ms per batch-32 forward pass) were obtained on a P100 datacentre GPU and should not be read as representative of edge or embedded deployment, where CPU- or microcontroller-class inference, memory bandwidth, and the recurrent branches' sequential (rather than fully parallelisable) computation pattern would all materially change achievable latency. We view genuine edge-feasibility validation as requiring dedicated on-device benchmarking rather than extrapolation from GPU timings, following the same domain-shift-aware, provenance-conscious evaluation discipline we have applied to TinyML vibration diagnostics in prior work [38]; we did not conduct that benchmarking here and flag it explicitly as outside this paper's scope rather than an implicit claim of edge readiness.

5.4. Implications for future PdM benchmarking practice and planned extensions

Beyond the specific results reported here, we suggest that the protocol ablation in Section 4.1 has a broader methodological implication for the sliding-window PdM literature: because splitting-protocol choice alone can move reported accuracy by more than 70 percentage points on identical data and an identical model, we argue that a leakage audit – reporting performance under at least a naive overlapping-window split and a chunk-based or otherwise leakage-controlled split – should become a standard reporting expectation for new RUL and fault-diagnosis benchmarks, in the same way that multi-seed variance reporting is now expected practice in general machine-learning benchmarking following work such as [27] and [26]. We believe this protocol, rather than any single reported accuracy figure, is the most durable and broadly reusable output of this study.

Two specific extensions remain as natural next steps building on the results in this paper. Section 4.4 already reports a controlled architectural ablation isolating each branch's contribution, including a dedicated attention-specific ablation, and Section 4.5 already reports a controlled identical-backbone single-task-vs-multi-task comparison; the two remaining extensions are: (i) a loss-weight sensitivity analysis over the classification/regression loss-weighting ratio, to establish whether the task-asymmetric instability reported in Section 4 can be partially mitigated by re-weighting rather than requiring additional data; and (ii) extending the cross-dataset comparison in Table 10 to additional public bearing benchmarks (e.g., PRONOSTIA/FEMTO, XJTU-SY, or Paderborn) to test whether the task-asymmetric instability pattern

reported here for NASA IMS Bearing generalises to other single-trial run-to-failure benchmarks or is specific to this dataset's label construction.

6. Conclusion

We show that the choice of train/test splitting protocol for sliding-window predictive maintenance benchmarks has a first-order, easily overlooked effect on reported performance, capable of inflating accuracy to a fabricated 99.9% or collapsing it to a degenerate 0% depending on how windows interact with the split boundary. Under a chunk-based, leakage-audited protocol that avoids both failure modes, an attention-enhanced multi-task architecture (AMTLNet) matches the strongest single-task baseline on NASA C-MAPSS while significantly outperforming naive multi-task training, demonstrating that multi-task learning's efficiency benefit – one model, two outputs – can be realised without a performance penalty when sufficient data is available. On two smaller, single-run benchmarks, the same architecture destabilises in a task-specific manner that correlates with label provenance rather than task type, a finding we translate into concrete guidance for practitioners evaluating multi-task PdM deployments under realistic data constraints. We release our leakage-audited splitting protocol as a reusable methodology for the broader sliding-window PdM research community.

Data Availability

NASA C-MAPSS (Turbofan Engine Degradation Simulation Data Set) and NASA IMS Bearing (Bearing Data Set) were originally released by the NASA Prognostics Center of Excellence (Saxena and Goebel, 2008; Lee et al.,

2007) and are publicly available via the PCoE Data Set Repository, https://www.nasa.gov/intelligent-systems-division/discovery-and-systems-health/pcoe/pcoe-data-set-repository/. For exact reproducibility, this study used the following Kaggle mirrors of the raw data: NASA C-MAPSS, https://www.kaggle.com/datasets/behrad3d/nasa-cmaps; NASA IMS Bearing, https://www.kaggle.com/datasets/vinayak123tyagi/bearing-dataset. The UCI Hydraulic System dataset ("Condition monitoring of hydraulic systems") is publicly available via the UCI Machine Learning Repository under a CC BY 4.0 licence, DOI: https://doi.org/10.24432/C5CW21 (Helwig, Pignanelli, and Schütze, 2015); the Kaggle mirror used in this study is available at https://www.kaggle.com/datasets/jjacostupa/condition-monitoring-of-hydraulic-sy Code implementing the leakage-audited chunk-based splitting protocol, the AMTLNet architecture, and all baseline, ablation, and identical-backbone comparison models is publicly available at https://github.com/iftitalukder/Leakage-Robust-Evaluation. This includes the reusable splitting-protocol implementation independent of the AMTLNet architecture, so that it can be adopted directly by other sliding-window PdM studies as recommended in Section 5.4.

Declaration of Competing Interest

The authors declare no competing financial interests or personal relationships that could have influenced the work reported in this paper.

Acknowledgments

This research did not receive any specific grant from funding agencies in the public, commercial, or not-for-profit sectors.

CRediT authorship contribution statement

Md Mahamudur Rahaman Shamim: Conceptualization, Software, Formal analysis, Writing - original draft. **Md. Nuruzzaman:** Investigation, Data curation, Validation. **Zannatul Ferdus:** Investigation, Visualization. **Md Rajib Ahmed:** Validation, Resources. **Abieer Nwshad Anwar:** Formal analysis, Writing - review & editing. **Mohammad Tooneer:** Resources, Writing - review & editing. **Johir Uddin Khan:** Writing - review & editing. **Khalid Hossen:** Supervision, Methodology.

Declaration of Generative AI and AI-assisted technologies in the writing process

During the preparation of this work, the author(s) used Claude (Anthropic) in order to improve language clarity and readability. After using this tool/service, the author(s) reviewed and edited the content as needed and take full responsibility for the content of the published article.

References

[1] S. Qiu, X. Cui, Z. Ping, N. Shan, Z. Li, X. Bao, X. Xu, Deep learning techniques in intelligent fault diagnosis and prognosis for industrial systems: A review, Sensors (2023). doi:10.3390/s23031305.

[2] W. Li, R. Huang, J. Li, Y. Liao, Z. Chen, G. He, R. Yan, K. Gryllias, A perspective survey on deep transfer learning for fault diagnosis in industrial scenarios: Theories, applications and challenges, Mechanical Systems and Signal Processing (2021). doi:10.1016/j.ymssp.2021.108487.

[3] C. E. Sunal, V. Dyo, V. Velisavljevic, Review of machine learning based fault detection for centrifugal pump induction motors, IEEE Access (2022). doi:10.1109/access.2022.3187718.

[4] R. Liu, B. Yang, A. Hauptmann, Simultaneous bearing fault recognition and remaining useful life prediction using joint-loss convolutional neural network, IEEE Transactions on Industrial Informatics (2020). doi:10.1109/tii.2019.2915536.

[5] S. Behera, R. Misra, A. Sillitti, Gan-based multi-task learning approach for prognostics and health management of iiot, IEEE Transactions on Automation Science and Engineering (2024). doi:10.1109/tase.2023.3267860.

[6] M. M. Abdelsamie, S. Azab, H. Hefny, Deep multi-task learning: a review of concepts, methods, and cross-domain applications, International Journal of Data Science and Analytics (2025). doi:10.1007/s41060-025-00892-y.

[7] S. Deng, J. Zhou, Prediction of remaining useful life of aero-engines based on cnn-lstm-attention, International Journal of Computational Intelligence Systems (2024). doi:10.1007/s44196-024-00639-w.

[8] C. Zhao, X. Huang, Y. Li, M. Iqbal, A double-channel hybrid deep neural network based on cnn and bilstm for remaining useful life prediction, Sensors (2020). doi:10.3390/s20247109.

[9] O. A. Ghoneim, A. Sleem, I. Gad, T. Allam, Remaining useful life prediction for turbofan engines using an attention-based data-driven deep-learning approach, PeerJ Computer Science (2025). doi:10.7717/peerj-cs.3438.

[10] B. Han, P. Yin, Z. Zhang, J. Wang, H. Bao, L. Song, X. Liu, H. Ma, D. Wang, Remaining useful life prediction of turbofan engines based on dual attention mechanism guided parallel cnn-lstm, Measurement Science and Technology (2024). doi:10.1088/1361-6501/ad8946.

[11] L. Wu, S. Song, H. Li, C. Hu, Y. Luo, Palc-net: A partial convolution attention-enhanced cnn-lstm network for aircraft engine remaining useful life prediction, Electronics (2025). doi:10.3390/electronics15010131.

[12] J.-w. Kim, K.-S. Park, Remaining useful life prediction of bearings via semi-supervised transfer learning based on an anti-self-healing health indicator, Sensors (2025). doi:10.3390/s25123662.

[13] S. Bisoyi, A. Rathi, S. Mahato, Fault diagnosis of rolling bearing failures using a multi-stage e-cnn-gru-sam network, Scientific Reports (2025). doi:10.1038/s41598-025-17008-y.

[14] Z. Wang, S. Yang, J. Mi, X. Zhao, Msran-ate: A novel hydraulic fault

diagnosis method fusing multi-scale attention and adaptive transformer, IEEE Access (2026). doi:10.1109/access.2026.3656928.

[15] N. Jafari, M. Farsangi, Physics-informed deep hidden markov model and wasserstein generative adversarial networks for hydraulic system condition monitoring, ISA Transactions (2026). doi:10.1016/j.isatra.2026.01.026.

[16] D. Kim, T.-Y. Heo, Anomaly detection with feature extraction based on machine learning using hydraulic system iot sensor data, Sensors (2022). doi:10.3390/s22072479.

[17] S. Kapoor, A. Narayanan, Leakage and the reproducibility crisis in machine-learning-based science, Patterns (2023). doi:10.1016/j.patter.2023.100804.

[18] L. Sasse, E. Nicolaisen-Sobesky, J. Dukart, S. Eickhoff, M. Götz, S. Hamdan, V. Komeyer, A. Kulkarni, J. Lahnakoski, B. C. Love, F. Raimondo, K. Patil, Overview of leakage scenarios in supervised machine learning, Journal of Big Data (2023). doi:10.1186/s40537-025-01193-8.

[19] R. Geirhos, J. Jacobsen, C. Michaelis, R. Zemel, W. Brendel, M. Bethge, F. Wichmann, Shortcut learning in deep neural networks, Nature Machine Intelligence (2020). doi:10.1038/s42256-020-00257-z.

[20] I. Tampu, A. Eklund, N. Haj-Hosseini, Inflation of test accuracy due to data leakage in deep learning-based classification of oct images, Scientific Data (2022). doi:10.1038/s41597-022-01618-6.

[21] M. Rosenblatt, L. Tejavibulya, R. Jiang, S. Noble, D. Scheinost, Data leakage inflates prediction performance in connectome-based machine learning models, Nature Communications (2024). doi:10.1038/s41467-024-46150-w.

[22] X. Yang, J. Li, X. Jiang, Research on information leakage in time series prediction based on empirical mode decomposition, Scientific Reports (2024). doi:10.1038/s41598-024-80018-9.

[23] C. An, Y. Park, S. Ahn, K. Han, H. Kim, S.-K. Lee, Radiomics machine learning study with a small sample size: Single random training-test set split may lead to unreliable results, PLoS ONE (2021). doi:10.1371/journal.pone.0256152.

[24] L. Schader, W. Song, R. Kempker, D. C. Benkeser, Don't let your analysis go to seed: on the impact of random seed on machine learning-based causal inference, Epidemiology (2024). doi:10.1097/ede.0000000000001782.

[25] F. Maleki, K. Ovens, R. Gupta, C. Reinhold, A. Spatz, R. Forghani, Generalizability of machine learning models: Quantitative evaluation of three methodological pitfalls, Radiology: Artificial Intelligence (2022). doi:10.1148/ryai.220028.

[26] P. Calle, A. Bates, J. C. Reynolds, Y. Liu, H. Cui, S. Ly, C. Wang, Q. Zhang, A. J. D. Armendi, S. S. Shettar, K. Fung, Q. Tang, C. Pan, Integration of nested cross-validation, automated hyperparameter optimization, high-performance computing to reduce and quantify the vari-

ance of test performance estimation of deep learning models, Computer Methods and Programs in Biomedicine (2025). doi:10.1016/j.cmpb.2025.109063.

[27] S. Banerjee, T. Marrinan, R. Cannon, T. Chiang, A. D. Sarwate, Measuring training variability from stochastic optimization using robust nonparametric testing, IEEE Journal of Selected Topics in Signal Processing (2024). doi:10.1109/jstsp.2025.3583140.

[28] H. Hewamalage, K. Ackermann, C. Bergmeir, Forecast evaluation for data scientists: common pitfalls and best practices, Data Mining and Knowledge Discovery (2022). doi:10.1007/s10618-022-00894-5.

[29] D. G. Lema, L. Sánchez-González, R. Usamentiaga, F. J. delaCalle, Benchmarking deep learning models for surface defect detection: a reproducible and statistically-rigorous approach, Journal of Intelligent Manufacturing (2025). doi:10.1007/s10845-025-02672-8.

[30] C. Li, S. Li, Y. Feng, K. Gryllias, F. Gu, M. Pecht, Small data challenges for intelligent prognostics and health management: a review, Artificial Intelligence Review (2024). doi:10.1007/s10462-024-10820-4.

[31] D. Wang, M. Zhang, Y. Xu, W. Lu, J. Yang, T. Zhang, Metric-based meta-learning model for few-shot fault diagnosis under multiple limited data conditions, Mechanical Systems and Signal Processing (2021). doi:10.1016/j.ymssp.2020.107510.

[32] A. Zhang, S. Li, Y. Cui, W. Yang, R. Dong, J. Hu, Limited data rolling

bearing fault diagnosis with few-shot learning, IEEE Access (2019). doi:10.1109/access.2019.2934233.

[33] J. Wu, Z. Zhao, C. Sun, R. Yan, X. Chen, Few-shot transfer learning for intelligent fault diagnosis of machine, Measurement (2020). doi:10.1016/j.measurement.2020.108202.

[34] X. Liang, M. Zhang, G. Feng, D. Wang, Y. Xu, F. Gu, Few-shot learning approaches for fault diagnosis using vibration data: A comprehensive review, Sustainability (2023). doi:10.3390/su152014975.

[35] H. Huang, D. Ye, L. Shen, W. Liu, Curriculum-based asymmetric multi-task reinforcement learning, IEEE Transactions on Pattern Analysis and Machine Intelligence (2022). doi:10.1109/tpami.2022.3223872.

[36] A. F. M. de Paula, I. Bensalem, D. Spina, P. Rosso, Mitigating the negative transfer in multi-task learning for harmful language detection in spanish and arabic, Expert Systems (2026). doi:10.1111/exsy.70182.

[37] H. Wang, X. Jin, Y. Du, N. Zhang, H. Hao, Adaptive hard parameter sharing method based on multi-task deep learning, Mathematics (2023). doi:10.3390/math11224639.

[38] K. Hossen, A systematic evaluation of domain shift effects in tinyml vibration diagnostics, Journal of Vibration Engineering & Technologies 14 (2026) 279. doi:10.1007/s42417-026-02511-x.

[39] K. Hossen, M. S. H. Chowdhury, M. H. Shihab, S. M. Aiyan, S. L. Rahman, M. Z. Hossen, Comparative evaluation of machine learning

algorithms for multiclass fault diagnosis of rotary compressors using triaxial vibration signals, in: 2025 International Conference on Quantum Photonics, Artificial Intelligence, and Networking (QPAIN), 2025, pp. 1–6. doi:10.1109/QPAIN66474.2025.11171877.

[40] N. Borst, W. Verhagen, Introducing cnn-lstm network adaptations to improve remaining useful life prediction of complex systems, The Aeronautical Journal (2023). doi:10.1017/aer.2023.84.

[41] Y. Fan, Y. Dang, Y. Guo, Fault identification model using convolutional neural networks with transformer architecture, Sensors (2025). doi:10.3390/s25133897.

[42] A. Saeed, M. A. Khan, U. Akram, W. J. Obidallah, S. Jawed, A. Ahmad, Deep learning based approaches for intelligent industrial machinery health management and fault diagnosis in resource-constrained environments, Scientific Reports (2025). doi:10.1038/s41598-024-79151-2.

[43] Y. Ji, A. Sun, J. Zhang, C. Li, A critical study on data leakage in recommender system offline evaluation, ACM Transactions on Information Systems (2020). doi:10.1145/3569930.

[44] J. A. Hernández López, B. Chen, M. Saad, T. Sharma, D. Varró, On inter-dataset code duplication and data leakage in large language models, IEEE Transactions on Software Engineering (2024). doi:10.1109/tse.2024.3504286.

[45] T. Miller, I. Durlik, A. Nowy, E. Kostecka, Smartbuildsim: An open-

source synthetic-twin framework for reproducible ai benchmarking in smart-building analytics, Sensors (2025). doi:10.3390/s25237263.

[46] T. Han, C. Liu, W. Yang, D. Jiang, Deep transfer network with joint distribution adaptation: A new intelligent fault diagnosis framework for industry application, ISA Transactions (2018). doi:10.1016/j.isatra.2019.08.012.

[47] J. Zhang, G. Pei, X. Zhu, X. Gou, L. Deng, L. Gao, Z. Liu, Q. Ni, J. Lin, Diesel engine fault diagnosis for multiple industrial scenarios based on transfer learning, Measurement (2024). doi:10.1016/j.measurement.2024.114338.